Fast-rising blue optical transients and AT2018cow following electron-capture collapse of merged white dwarfs

Lyutikov, M.; Toonen, S.

DOI
10.1093/mnras/stz1640

Publication date
2019

Document Version
Final published version

Published in
Monthly Notices of the Royal Astronomical Society

Monthly Notices
of the
ROYAL ASTRONOMICAL SOCIETY

MNRAS **487,** 5618–5629 (2019) doi:10.1093/mnras/stz1640

Fast-rising blue optical transients and AT2018cow following electron-capture collapse of merged white dwarfs

Maxim Lyutikov[1]★ and Silvia Toonen[2]

[1]*Department of Physics and Astronomy, Purdue University, 525 Northwestern Avenue, West Lafayette, IN 47907-2036, USA*
[2]*Anton Pannekoek Institute for Astronomy, University of Amsterdam, PO Box 94249, 1090 GE, Amsterdam, the Netherlands*

Accepted 2019 June 9. Received 2019 June 7; in original form 2019 February 4

ABSTRACT

We suggest that fast-rising blue optical transients (FBOTs) and the brightest event of the class, AT2018cow, result from an electron-capture collapse to a neutron star following the merger of a massive ONeMg white dwarf (WD) with another WD. Two distinct evolutionary channels lead to the disruption of the less-massive WD during the merger and the formation of a shell-burning non-degenerate star incorporating the ONeMg core. During the shell-burning stage, a large fraction of the envelope is lost to the wind, while mass and angular momentum are added to the core. As a result, the electron-capture collapse occurs with a small envelope mass, after $\sim 10^2$–10^4 yr. During the formation of a neutron star, as little as $\sim 10^{-2}\,M_\odot$ of the material is ejected at the bounce-off with mildly relativistic velocities and total energy of about a few 10^{50} erg. This ejecta becomes optically thin on a time-scale of days – this is the FBOT. During the collapse, the neutron star is spun up and the magnetic field is amplified. The ensuing fast magnetically dominated relativistic wind from the newly formed neutron star shocks against the ejecta, and later against the wind. The radiation-dominated forward shock produces the long-lasting optical afterglow, while the termination shock of the relativistic wind produces the high-energy emission in a manner similar to pulsar wind nebulae. If the secondary WD was of the DA type, the wind will likely have $\sim 10^{-4}\,M_\odot$ of hydrogen; this explains the appearance of hydrogen late in the afterglow spectrum. The model explains many of the puzzling properties of FBOTs/AT2018cow: host galaxies, a fast and light anisotropic ejecta producing a bright optical peak, afterglow high-energy emission of similar luminosity to the optical, and late infrared features.

Key words: stars: neutron – supernovae: general – white dwarfs.

1 INTRODUCTION

AT2018cow (Prentice et al. 2018; Smartt et al. 2018; Ho et al. 2019; Margutti et al. 2019; Perley et al. 2019) is a mysterious astrophysical event. It is likely to be the brightest member of the class of fast-rising blue optical transients (FBOTs; Drout et al. 2014). AT2018cow seems to be at a critical point of supernova explosions (and associated complicated nuclear reactions, neutrino transports physics), pulsars/magnetars, (early) pulsar wind nebulae (PWNe), possibly gamma ray bursts (GRBs) and, as we suggest in this paper, the physics of white dwarf (WD) binaries.

AT2018cow has a few surprising features, the most important of which, in our view, are the following:

(i) an optical rise-time of $\leq$3 d, which is an order of magnitude shorter than the conventional Ni-powered supernovae;

(ii) a peak optical luminosity $\sim 4 \times 10^{44}$ erg s^{-1}, which exceeds the typical peak power of supernovae;

(iii) X-ray emission of initial power $\sim 10^{43}$ erg s^{-1}, with an extra component at $t \leq 15$ d, peaking at $\sim$40 keV (see fig. 6 in Margutti et al. 2019);

(iv) a clear change of the properties of the emission at $\sim$ 20 d (see fig. 9 in Margutti et al. 2019);

(v) an indication of the rising infrared (IR) component at $t \geq 30$ d (see fig. 5 in Perley et al. 2019);

(vi) bright radio emission $t \geq 80$ d, peaking at $\sim 10^{10}$ Hz (see fig. 11 in Margutti et al. 2019).

These properties exclude normal Ni-powered supernovae and require a separate formation channel. We discuss one such possible channel in the present paper, in an attempt to build a coherent model of AT2018cow.

★ E-mail: lyutikov@purdue.edu

2 THE MODEL: A SPECIFIC CHANNEL OF WD MERGERS

In this paper, we discuss a scenario where FBOTs are powered by the electron-capture collapse following a merger of a massive ONeMg WD with another WD. Previously, the electron-capture collapse was mostly used in accretion models (Canal & Schatzman 1976), hence the name accretion induced collapse (AIC; see also Miyaji et al. 1980; Nomoto & Kondo 1991; Timmes & Woosley 1992; Kitaura, Janka & Hillebrandt 2006; Jones et al. 2016). Some details of binary evolution and of the collapse in such systems were previously discussed by Lyutikov & Toonen (2017); see also Schwab, Quataert & Bildsten (2016), Brooks et al. (2017), Yungelson & Kuranov (2017), Toonen et al. (2018) and Ruiter et al. (2019).

Let us outline the main stages; see Lyutikov & Toonen (2017) for a more detailed discussion, and also Ruiter et al. (2019). An initial system with a primary mass $M_1 \sim 6$–$10\,\mathrm{M}_\odot$ and a secondary mass $M_2 \sim 3$–$6\,\mathrm{M}_\odot$ forms via two distinct evolutionary channels a double degenerate CO–ONeMg WD system. For a sufficiently large mass ratio $q \equiv M_2/M_1 > q_{\rm crit} \sim 0.25$ (Marsh, Nelemans & Steeghs 2004), the ensuing gravitational wave-driven mass transfer is unstable, whereby the less-massive CO WD is disrupted on a few orbital time-scales and forms a disc around the primary. Note that possible detonation of the CO WD secondary would eject a small amount of mass, leaving the ONeMG core mostly intact (Kashyap et al. 2018). Disc accretion at high rates creates a spreading layer – a belt-like structure on the surface of the primary (Inogamov & Sunyaev 1999; Balsara et al. 2009; Inogamov & Sunyaev 2010; Belyaev, Rafikov & Stone 2013; Philippov, Rafikov & Stone 2016). After the spreading is complete on viscous time-scale of $\sim 10^4$ s (e.g. Shen et al. 2012), the resulting star of $\sim 2\,\mathrm{M}_\odot$ consists of a slowly rotating degenerate ONeMg core and a non-degenerate envelope, rotating with a period of hundreds of seconds. The non-degenerate envelope expands to $R_* \sim$ a few 10^9 cm. The star will emit near the Eddington limit and drive powerful winds. Angular momentum contained in the shell will be both lost to the wind and transported to the core through the (turbulent) boundary layer.

The merger product ignites shell CO burning, adding mass to the degenerate core; at the same time, mass and angular momentum are lost due to powerful winds. For an ONeMg WD sufficiently close to the Chandrasekhar mass, an electron-capture/AIC follows after $\sim 10^2$–10^4 yr. During the collapse, the magnetic field is amplified (Mösta et al. 2015), and the neutron star (NS) is spun to millisecond periods.

To estimate the resulting magnetic field and the spin frequency, we note that during the collapse of a core rotating initially with a spin frequency Ω and collapsing by a factor $\eta_{\rm c} \sim 100$ (from a few thousand to a few tens of kilometres), the final NS will rotate with $\omega_{\rm c} \sim \eta_{\rm c}^2 \Omega$. The ratio $\omega/\Omega = \eta_{\rm c}^2 \sim 10^4$ also estimates by how much the magnetic field is twisted during the collapse.

Thus, the final toroidal magnetic field can be $\sim 10^4$ times higher than the poloidal magnetic field. In addition, the poloidal magnetic field will be amplified by flux conservation. For example, if we start with $B_{\rm WD} \sim 10^6$ G, flux conservation will give a factor $\eta_{\rm c}^2 \approx 10^4$, while differential rotation will further boost that by $\sim 10^4$, reaching magnetar-like values of $B \geq B_{\rm Q}$, $B_{\rm Q} = m_{\rm e}^2 c^3/(e\hbar)$.

As a result, the newly born spinning NS will produce a long-lasting relativistic wind, which first shocks against the ejecta material and later on against the wind material lost during the shell-burning stage. The highly magnetized relativistic wind produced by a central NS will interact with the fairly dense newly ejected material and dense pre-AIC wind, producing an X-ray afterglow at the highly magnetized reverse shock, in a way similar to the case of afterglows from long GRBs, as suggested by Lyutikov & Camilo Jaramillo (2017).

Fig. 1 shows the immediate surrounding of an FBOT at times of ∼days to weeks after the collapse. This picture is our working model.

The key point of the model is that a merger of a heavy ONeMg WD with another WD, and ensuring mass loss during the shell-burning stage, results in the collapse of the core surrounded by a fairly light envelope, tens of per cent of $\mathrm{M}_\odot$ at most. Depending on the particular collapse time, few cases are expected when the AIC occurs right before the shell-burning is about to end. This would produce fast ejecta with small mass and would lead to AT2018cow-like events. In other cases, envelopes of a few tenths of solar masses are ejected, producing longer and less bright transients, which are still fast and luminous if compared with conventional supernovae.

In addition to spinning up the core, a large amount of angular momentum of the shell (disrupted secondary WD) is lost to the wind. As a result, the AIC can be direct, without formation of the accretion disc. In this case, the newly born NS loses most of its rotational energy to the fast, relativistic wind. For a shorter shell-burning stage, there is too much angular momentum in the shell, which leads to the formation of the accretion disc that spins down the central NS in a propeller stage. As a result, a large fraction of the energy is deposited into relatively slow, matter-dominated wind with low radiation efficiency.

3 THE PRE-COLLAPSE WIND AND THE EJECTA

3.1 Pre-collapse wind

Let us assume that the post-merger/shell-burning star launches a wind with velocity $V_{\rm w}$. After time $t_{\rm w}$, the edge of the wind reaches radius $r_{\rm max} = R_* + V_{\rm w} t_{\rm w}$. For a total mass in the wind $M_{\rm env}$, we find

$$\rho_{\rm w} = \frac{\dot{M}}{4\pi r^2 V_{\rm w}}$$

$$M_{\rm env} = \int_{R_*}^{R_* + V_{\rm w} t_{\rm w}} \rho_{\rm w} 4\pi r^2 \,{\rm d}r = \dot{M} t_{\rm w} \qquad (1)$$

$$t_{\rm w} = \frac{M_{\rm env}}{\dot{M}}.$$

For mass loss rate of $\dot{M} = 10^{-3}\,\mathrm{M}_\odot\ \mathrm{yr}^{-1}$ and total mass in the envelope of $\sim 0.5\,\mathrm{M}_\odot$, this stage lasts $t_{\rm w} \sim 5 \times 10^2$ yr; we adopt the notation $x_n = X/10^n$.

The optical depth to Thomson scattering through the wind is ∼1 at

$$r_{\rm w} = \frac{\sigma_R \dot{M}}{4\pi m_{\rm p} V_{\rm w}} = 2 \times 10^{13}\, \dot{m}_{-3} V_{\rm w,8}^{-1}\,\mathrm{cm}. \qquad (2)$$

In fact, the wind is composed of the WD material rich in heavy elements. Thus, its opacity is similar to the case of Type Ia supernovae – it is dominated by line transitions, in expanding wind and can be an order of magnitude higher than free–free scattering (Karp et al. 1977; Höflich, Wheeler & Thielemann 1998; Pinto & Eastman 2000).

3.2 Ejecta

As the shell is accreted on to the proto-neutron star, a narrow outer layer will be ejected. Studies of the AIC-ejected mass predict

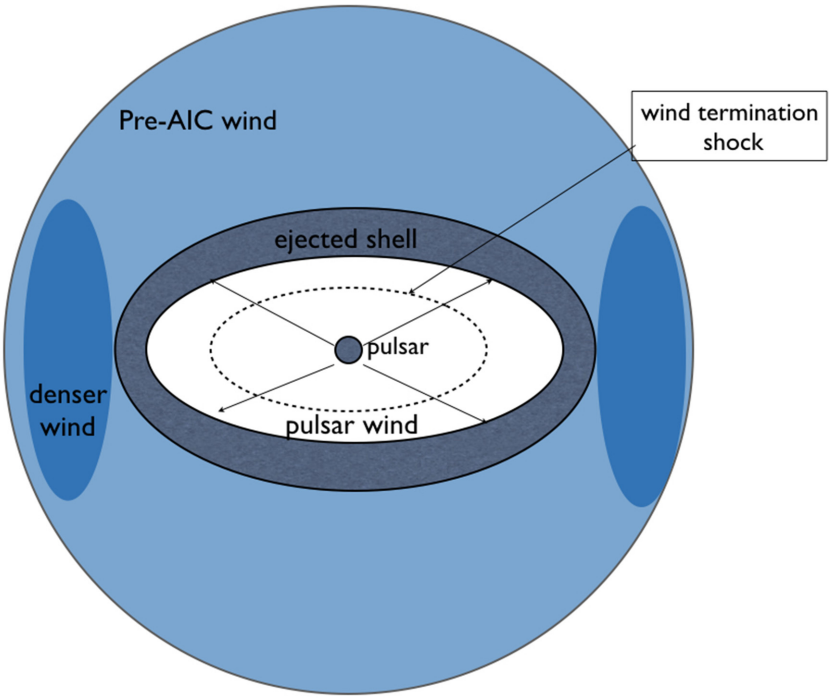

Figure 1. Immediate surroundings of an FBOT: the remaining NS generates anisotropic pulsar-like wind (highly relativistic, highly magnetized with power $\sim\sin^2\theta$), which interacts with the bounced-ejected shell, and the preceding wind from the shell-burning stage. The pulsar winds, the ejected shell and the pre-explosion wind are all expected to be equatorially collimated.

$\sim 10^{-3}$–$10^{-1}\,\mathrm{M}_\odot$ ejected (Woosley & Baron 1992; Fryer et al. 1999; Abdikamalov et al. 2010; Sharon & Kushnir 2019).

These studies were mostly concerned with single degenerate scenario of AIC, basically with no envelope. It is not clear how the presence of a tenuous envelope, of a few $0.1\,\mathrm{M}_\odot$, would affect the ejecta mass. Let us assume, for a particular case of AT2018cow, a bounced ejected mass of $M_{\rm ej}$, with maximal velocity $V_{\rm ej,\,0}$. For homologous expansion with $v \propto r$, the energy in the ejected part is

$$E_{\rm ej} = \frac{3}{10} M_{\rm ej} V_{\rm ej,0}^2. \tag{3}$$

Before the ejecta slows down as a result of the interaction with the pre-existing wind, its density evolves according to

$$\rho_{\rm ej} = \frac{3}{4\pi}\frac{M_{\rm ej}}{(V_{\rm ej,0} t_{\rm ej})^3}, \tag{4}$$

where $V_{\rm ej,\,0}$ is the maximum velocity of the ejecta.

For numerical estimates, we chose $M_{\rm ej} \approx 10^{-2} m_{\rm ej,-2}\,\mathrm{M}_\odot$ (many of the final relations depend weakly on ejecta mass, $\propto M_{\rm ej}^{1/4}$; e.g. equations 21 and 23). The velocity of the ejecta will be related to the escape velocity from the proto-NS,

$$V_{\rm ej,0} \approx \sqrt{\frac{G M_{\rm NS}}{R_{\text{proto-NS}}}} = 7\times 10^9\,\mathrm{cm\,s^{-1}} = 0.26c, \tag{5}$$

for a proto-NS radius of $R_{\text{proto-NS}} = 30\,\mathrm{km}$. The ejecta energy is then $E_{\rm ej} \approx 4\times 10^{50} m_{\rm ej,\,-2}$ erg. Thus, our model naturally produces fast and light ejecta.

3.3 Ejecta–wind interaction

The ejecta will launch a forward shock into the pre-explosion wind. As the shock propagates through the wind, the accumulated mass is then

$$M_{\rm acc} \approx \dot{M} t \frac{V_{\rm ej,0}}{V_{\rm w}}. \tag{6}$$

This becomes equal to the ejecta mass at

$$t_{\rm slow} = \frac{M_{\rm ej}}{\dot{M}}\frac{V_{\rm w}}{V_{\rm ej,0}} \to 4\times 10^6 m_{\rm ej,-2} V_{\rm w,8} \dot{m}_{-3}^{-1}\,\mathrm{s}. \tag{7}$$

Thus, the external wind has little effect on the ejecta until approximately a month after the explosion. Before that, the ejecta is in the free expansion stage.

This will be approximately the time that the NS-driven shock exits the ejecta and enters the wind. We associate this with the transition of the afterglow properties at $\sim$20 d (Margutti et al. 2019).

4 OPTICAL TRANSIENT

4.1 Optical emission I: expansion of the ejecta

As discussed by Drout et al. (2014), fast optical transients can be powered either by the thermal energy of a low-mass ejected envelope or by the central engine. In the first case, the Thomson optical depth through ejecta is

$$\tau_{\rm ej} = \frac{\rho_{\rm ej}}{m_{\rm p}}\sigma_{\rm T} V_{\rm ej,0} t = \frac{3}{4\pi}\frac{M_{\rm ej}\sigma_{\rm T}}{m_{\rm p}(V_{\rm ej,0} t)^2} = 3 m_{\rm ej,-2} t_{\rm d}^{-2}, \tag{8}$$

where $t_{\rm d}$ is time in days since the explosion. The surface $\tau = 1$ evolves with time according to

$$r_{{\rm ej},\tau=1} = V_0 t\left(1 - \frac{2\pi}{5}\frac{m_{\rm p} V_0^4}{E_{\rm ej}\sigma_{\rm T}}\right). \tag{9}$$

It reaches maximum at

$$t_{\rm ej,max} = \sqrt{\frac{5}{6\pi}}\sqrt{E_{\rm ej}\sigma_{\rm T}m_{\rm p}V_0^4} \approx 1 m_{\rm ej,-2}^{1/2}\,{\rm d}$$

$$r_{\rm ej,max} = \sqrt{\frac{10}{27\pi}}\sqrt{E_{\rm ej}\sigma_{\rm T}m_{\rm p}V_0^2} \approx 5\times10^{14} m_{\rm ej,-2}^{1/2}\,{\rm cm}. \quad (10)$$

This explains the short rise time of the transient. Also, note that the radius in equation (10) is larger than the radius in equation (2) when the wind becomes optically thin. Thus, the maximum of the ejecta emission is not affected by scattering in the pre-explosion wind.

In fact, for the expanding optically thick plasma, the peak in luminosity will appear before the shell becomes optically thi,n because photons diffuse out faster (Arnett 1982). The peak time is

$$t_{\rm pk} \approx \sqrt{\frac{M_{\rm ej}\kappa}{4\pi V_{\rm ej,0}c}} \approx 0.4 m_{\rm ej,-2}\,{\rm d}, \quad (11)$$

where $\kappa \approx 0.1$ cm^2 g^{-1} is an estimate of the effective opacity due to electron scattering. Estimates (8) and (11) explain the short rise time of the optical light curve.

The free–free emission of the optically thin part of the ejecta is fairly small,

$$L_{\rm ej,ff} \approx j_{\rm ff} n_{\rm ej}^2 (V_{\rm ej,0}t)^3 = 4\times10^{39}\,{\rm erg\,s^{-1}} m_{\rm ej,-2}^2 T_4^{1/2} t_{\rm d}^{-3},$$

$$j_{\rm ff} = 2.4\times10^{-27}\sqrt{T}n^2, \quad (12)$$

where $j_{\rm ff}$ is free–free emissivity (Lang 1999). Thus, we associated the early fast optical transient with the emission of the ejected shell.

4.2 Optical emission II: forward shock from the NS-driven wind

The NS wind is shocked at the termination shock and will also produce a forward shock. Similar amounts of energy will be dissipated in both shocks. Particles accelerated at the termination shock produce the non-thermal X-ray emission, while the forward shock will produce the long-lasting optical emission (in addition to the emission produced by the ejecta).

Let us first consider the forward shock emission. The forward shock initially propagates through the ejecta and, later, through the pre-explosion wind. The shock driven by the NS wind will be modified by radiation pressure (Weaver 1976; Budnik et al. 2010; Ofek et al. 2010; Lyutikov 2018). The observed properties of mildly relativistic shocks are fairly complicated and often depend greatly on the underlying parameters because of the high dependence of photon production rates, photon escape and pair production on the plasma properties. Qualitatively, radiation-dominated shocks can temporarily reach a temperature that exceeds the shock jump conditions (even taking into account radiation pressure). For fast photon production, this can result in isothermal jumps (Landau & Lifshitz 1959; Lyutikov 2018), in which case the peak temperature exceeds the final temperature by a factor of a few. For slow photon production, the temperature peak can exceed the final temperature by a large amount (Ioka, Levinson & Nakar 2018; Ito et al. 2018).

Here, we give an order-of-magnitude estimate of the final post-shock temperature in strongly radiationally dominated shock. The post-shock pressure is

$$p_{\rm FS} \sim \frac{L_{\rm w}}{4\pi R_{\rm PWN}^2 c} = \frac{\sqrt{3}}{16\pi}\frac{\sqrt{L_{\rm w,0}M_{\rm ej}}}{\sqrt{c}V_{\rm ej,0}^{3/2}t^{5/2}}, \quad (13)$$

which has contributions from both matter pressure $\sim nT$ and radiation pressure $\sim 4\sigma_{\rm SB}T^4/c$. Radiation pressure dominates for (Weaver 1976; Budnik et al. 2010; Ofek et al. 2010; Lyutikov 2018)

$$V_{\rm s} \gg \frac{(\rho\lambda_{\rm C}^3)^{1/6}c}{m_{\rm e}\mu^{2/3}} \approx 10^5 m_{\rm ej,-2}^{1/6} t_{\rm d}^{-1/2}\,{\rm cm\,s^{-1}}, \quad (14)$$

where $\lambda_C = \hbar/(m_e c)$ and $\mu = m_{\rm p}/m_{\rm e}$. Comparing with the relative velocity of the shock with respect to the ejecta, equation (22), we conclude that the forward shock is radiation-dominated with post-shock temperature (far downstream):

$$T_{\rm FS} \approx \left(\frac{cL_{\rm w,0}M_{\rm ej}}{\sigma_{\rm SB}^2 V_{\rm ej,0}^3 t^5}\right)^{1/8} = 4\times10^4\, m_{\rm ej,-2} t_{\rm d}^{-5/8}\,{\rm K}. \quad (15)$$

This matches the observed temperatures at early times, in both value and (presumably) the temporal decrease (Margutti et al. 2019).

However, radiation-dominated shocks require sufficiently high optical depth, at least of the order of $\tau \sim c/V_{\rm s}$, while final stationary configurations can be reached at optical depths of thousands (Ioka et al. 2018). This is not really satisfied in the particular case: from $r\sigma_{\rm T}n \sim c/V_{\rm s}$, with $V_{\rm s}$ given by equation (22) and density by equation (4), the condition $\tau \sim c/V_{\rm s}$ is satisfied for

$$t \le \frac{L_{\rm w,0}^{1/3}M_{\rm ej}^{1/3}\sigma_{\rm T}^{2/3}}{m_{\rm p}^{2/3}cV_0} = 0.1 m_{\rm ej,-2}^{1/3}\,{\rm d}. \quad (16)$$

Thus, it is only at very early times that the shock is highly radiation-dominated.

At the moment of shock breakout we expect an X-ray flash with a duration given by equation (16) and luminosities of $\sim 10^{42}$–10^{43} erg s^{-1} (e.g. Svirski & Nakar 2014). Later, after the shock is no longer radiation dominated, the post-shock temperature evaluates to

$$T_{\rm s} = \frac{3}{16}m_{\rm p}V_{\rm s}^2 \approx \frac{m_{\rm p}L_{\rm w,0}^{1/2}V_0^{3/2}\sqrt{t}}{\sqrt{cM_{\rm ej}}} = 5\times10^5 t_{\rm d}^{1/2} m_{\rm ej,-2}^{-1/2}\,{\rm eV}. \quad (17)$$

The corresponding free–free luminosity is far too small $\sim 10^{35} m_{\rm ej,-2}^{7/4} t_{\rm d}^{-11/4}$ erg s^{-1}.

4.3 Anisotropy

Thus, optical emission is puzzling: it is hard to see how the requirement for radiation-modified shocks (and hence large optical depth) can be reconciled with short transient time-scales (and hence small optical depth). A possible answer is anisotropy. All the ingredients (e.g. pre-collapse wind, ejecta and the NS wind) are expected to be anisotropic (see Fig. 1). First, the wind is launched by a star that rotates with nearly critical velocity. Even solar wind is highly anisotropic: slow and dense in the equatorial sector and fast in the polar regions (with approximately constant $d\dot{M}/d\Omega$). Second, the newly formed NS can, under certain parameters, be nearly critically spinning, so that the ejecta is also anisotropic (see Lyutikov & Toonen 2017). Third, the remaining wind of the NS is equatorially collimated, with power $\propto \sin^2\theta$ (Michel 1973).

There are strong observational arguments in favour of anisotropy. First, hydrogen and helium lines show spectral asymmetry, with a tail towards longer wavelengths (Margutti et al. 2019). This can be explained if the line of sight samples the ejecta unevenly.

Anisotropic ejecta can also reconcile the requirements of low ejecta mass, $\sim 10^{-2}\,{\rm M}_\odot$ (and hence early transparency) and the requirement of larger ejecta mass, to keep the NS wind-generated forward shock to be radiatively dominated; this would be a good explanation of the optical temperature (see equation 15).

An alternative possibility is that the later optical emission originates as synchrotron emission from particles accelerated at the forward shock. It is possible to construct a model of particle acceleration at the forward shock following the standard GRB parametrization (e.g. Piran 2004), with $\epsilon_B \sim 10^{-4}$, $\gamma \sim 10^3$, in the fast cooling regime (fast cooling for the forward shock is important, and X-ray luminosity for the termination shock and optical from the forward shock are comparable; Margutti et al. 2019). However, the expected spectrum will be non-thermal.

5 NON-THERMAL EMISSION IN FBOTS: PULSAR-LIKE TERMINATION SHOCK IN FAST NS WIND

5.1 Wind power

The newly created NS is spun up to short periods and the magnetic field is amplified. The central NS will produce a highly magnetized wind that shocks against the ejecta (and, later, against the pre-explosion wind). The NS wind–ejecta interaction will produce two shocks: forwards shock in the ejecta and a termination shock in the wind. It is the wind termination shock that produces the X-ray emission, while the radiation-dominated forward shock produces the optical transient (see Section 4.2). In the termination shock, the accelerated particles will produce synchrotron emission in the fast cooling regime, so that a large fraction of the wind power will be emitted as radiation. (See Lyutikov & Camilo Jaramillo 2017, for a discussion of emission produced at the highly magnetized termination shock in GRBs.)

In the fast cooling regime, most of the power given to the accelerated particles is emitted. Let us then identify the observed X-ray luminosity with NS wind power. It is nearly constant at $L_0 \approx 10^{43}$ erg s^{-1} until $t_\Omega \sim 20$ d and then falls $\propto t^{-2}$ (see fig. 5 in Margutti et al. 2019). Using the initial pulsar spin-down power and spin-down time t_Ω, we find the magnetic field and the initial spin:

$$B_{\rm NS} \approx \frac{c^{3/2} I_{\rm NS}}{\sqrt{L_0} R_{\rm NS}^3 t_\Omega} = 8 \times 10^{14}\,{\rm G};$$

$$\Omega_0 = \sqrt{\frac{L_0 t_\Omega}{I_{\rm NS}}} = 140\,{\rm rad\,s^{-1}}. \tag{18}$$

At $t > t_\Omega$, we have $L \propto t^{-2}$. Thus, we suggest that a magnetar-type object is formed; its initial spin is not very high (i.e. 45 ms). The wind power at time t is then

$$L_{\rm w} = \frac{L_{\rm w,0}}{(1 + t/t_\Omega)^2}. \tag{19}$$

In fact, because observed X-ray luminosity is a lower limit on wind power, the estimates in equation (18) are upper limits on the magnetic field and lower limits on the initial spin.

The dynamics of shock driven by the wind with power (19) will depend on two factors: spin-down time t_Ω and whether the shock is in the ejecta (see Section 5.2), or in the pre-explosion wind (see Section 5.3). We consider these two cases next.

5.2 Propagation of NS wind-driven shock through the ejecta

The newly formed NS generates a powerful wind that first propagates within the ejecta and, later, through the pre-explosion wind. Let us consider the dynamic of the wind-driven shock propagating through the ejecta with density (4). In the Kompaneets approximation (Kompaneets 1960; Bisnovatyi-Kogan & Silich 1995),[1] the relativistic wind with power $L_{\rm w}$ will produce a cavity expanding according to

$$\frac{L_{\rm w}}{4\pi R^2 c} = \rho_{\rm ej} \left(\partial_t R - \frac{R}{t}\right)^2. \tag{20}$$

Given the wind power (19) and density (4), the radius of the cavity evolves according to

$$R_{\rm PWN} \approx \frac{(L_{\rm w,0} t_\Omega)^{1/4} V_{\rm ej,0}^{3/4}}{(c M_{\rm ej})^{1/4}} t \sqrt{\arctan\sqrt{t/t_\Omega}}$$

$$= \begin{cases} \dfrac{L_{\rm w,0}^{1/4} V_{\rm ej,0}^{3/4}}{(c M_{\rm ej})^{1/4}} t^{5/4}, & t \to 0 \\ \sqrt{\dfrac{\pi}{2}} \dfrac{(L_{\rm w,0} t_\Omega)^{1/4} V_{\rm ej,0}^{3/4}}{(c M_{\rm ej})^{1/4}} t, & t \to \infty \end{cases} \tag{21}$$

(function $x\sqrt{\arctan\sqrt{x}}$ has limits $x^{5/4}$ for $x \ll 1$ and $\sqrt{\pi/2}x$ for $x \gg 1$). For example, at 1 d, the NS produces a cavity of size $R \approx 6 \times 10^{13} m_{\rm ej,-2}^{-1/4}$.

The relative velocity of the shock with respect to the ejecta is

$$V_{\rm s} = 0.37 \frac{(L_{\rm w,0} t)^{1/4} V_{\rm ej,0}^{3/4}}{(c M_{\rm ej})^{1/4}} = 2 \times 10^8\, t_{\rm d}^{1/4} m_{\rm ej,-2}^{1/4}\,{\rm cm\,s^{-1}}. \tag{22}$$

Thus, it changes only slowly with time.

The corresponding equipartition post-termination shock magnetic field (in the highly magnetized wind) is

$$B = \frac{\sqrt{2 L_w}}{\sqrt{c} R} = \sqrt{2} \frac{L_{w,0}^{1/4} M_{ej}^{1/4}}{c^{1/4} V_{ej,0}^{3/4}} \left(t^{5/4} \sqrt{1 + t/t_\Omega}\right)^{-1}$$

$$\approx 300{\rm G} m_{ej,-2}^{1/4} \left(t_d^{5/4} \sqrt{1 + 0.05 t_d}\right)^{-1} \tag{23}$$

($t_{\rm d}$ is time measured in days). Thus, at early times, the magnetic field $B \propto t^{-5/4}$, while later $B \propto t^{-7/4}$.

Also, note that the NS-driven shock never overtakes the freely expanding ejecta (radius 21 is always smaller than $V_{\rm ej,0} t$). The shock breaks out hydrodynamically from the ejecta into the pre-existing wind when ejecta starts to decelerate at equation (7), after approximately a month.

5.3 Propagation of NS wind-driven shock through pre-explosion wind

The Kompaneets approximation (20), in the pre-explosion wind profile (1) takes the form (see Appendix A for comparison with Sedov scaling – the resulting relations are similar)

$$\frac{L_{\rm w}}{4\pi R^2 c} = \rho_{\rm w} \left(\partial_t R - v_{\rm w}\right)^2. \tag{24}$$

Using the wind power (19), equation (24) gives

$$R_{\rm PWN} = t v_{\rm w} + \sqrt{\frac{L_{\rm w,0} v_{\rm w}}{c \dot{M}}} t_\Omega \ln(1 + t/t_\Omega) \approx \sqrt{\frac{L_{\rm w,0} v_{\rm w}}{c \dot{M}}} t. \tag{25}$$

[1]The Kompaneets approximation assumes supersonic driving, while Sedov scaling assumes subsonic driving of the expansion. At early times, when the termination shock is close to the contact discontinuity, the Kompaneets approximation is more justified that the Sedov approximation.

Here, the last relation assumes $t \ll t_\Omega$ and high shock velocity $V_s \gg v_w$:

$$V_s = \sqrt{\frac{L_{w,0} v_w}{c\dot{M}}} = 7 \times 10^8 V_{w,8}^{1/2} \dot{m}_{-3}^{-1/2} \,\mathrm{cm\,s^{-1}}. \quad (26)$$

The equipartition magnetic field is

$$B \approx \frac{\sqrt{2L_w}}{\sqrt{c}R} = \sqrt{\frac{2\dot{M}}{v_w}} \frac{1}{t(1+t/t_\Omega)}. \quad (27)$$

Thus, at later times, for $t \gg t_\Omega$ the magnetic field decreases $\propto t^{-2}$ (one power of time comes from the radius increasing nearly linearly with time, and another from decreasing central power).

5.4 The X-ray continuum and late near-infrared bump: synchrotron emission from the NS-driven termination shock

There are two separate components in the early X-ray spectrum: at $t_d \sim 7$, an early X-ray bump at ∼50 keV and a continuous power law. The bump disappeared later, while the continuous component did not show significant spectral evolution in the 0.3–10 keV spectrum during the two months (Rivera Sandoval et al. 2018). In addition, after ∼40 d, there was an increase in the near-infrared (NIR) emission.

The continuous component is generally consistent with the synchrotron cooled population, resulting in the spectral index $\alpha \approx 0.5$. We associate the X-ray emission with the particles accelerated at the termination shock emitting in the fast cooling regime.

Suppose the NS-launched wind is propagating with Lorentz factor γ_w. Then, using the estimates of the magnetic field (23) and (27), the peak synchrotron frequency of particles accelerated by the wind termination shock is

$$\epsilon_s \approx \gamma_w^2 \hbar \frac{eB}{m_e c} = \begin{cases} \sqrt{2}\frac{e\hbar}{m_e c^{5/4}} \gamma_w^2 \frac{L_{w,0} M_{ej}^{1/4}}{V_{ej,0}^{3/4}} \left(t^{5/4}\sqrt{1+t/t_\Omega}\right)^{-1} \\ \quad = 50\,\mathrm{keV}\, m_{ej,-2}^{1/4} \gamma_{w,5}^2 \left(t_d^{5/4}\sqrt{1+0.05t_d}\right)^{-1} \\ \frac{e\hbar}{m_e c} \gamma_w^2 \sqrt{\frac{\dot{M}}{v_w}} \left(t(1+t/t_\Omega)\right)^{-1} \\ \quad = 50\,\mathrm{keV}\, \dot{m}_{-3}^{1/2} v_{w,8} \gamma_{w,5}^2 \left(t_d\sqrt{1+0.05t_d}\right)^{-1} \end{cases}, \quad (28)$$

where t_d is the time since the explosion in days. The first line corresponds to times when the shock is in the ejecta, while the second is when it is in the wind.

The cooling energy is

$$\epsilon_c \approx \frac{\hbar m_e^5 c^9}{e^7 B^2 t^2}. \quad (29)$$

Initially, it is very small, well below the injection frequency (28). As a result, a cooled distribution will form below the injection peak, producing a power-law spectrum with $\alpha \approx 0.5$. This is the origin of the persistent component. In the fast cooling regime, the particle distribution below the injection peak is independent of the above-the-peak power-law distribution. This explains the constant 0.3–10 keV spectrum (Rivera Sandoval et al. 2018), even for varying luminosity.

Later, with the magnetic field in the termination shock decreasing $\propto t^{-2}$ (see equation 27), the cooling energy increases sharply with time,

$$\epsilon_c \approx \frac{m_e^5 c^9 \hbar}{e^7} \frac{v_w^{3/2}}{\dot{M}^{3/2} t_\Omega^3} t^4. \quad (30)$$

(This is also a sensitive function of the parameters.) For faster ($v_w \sim 10^9$ cm s^{-1}) and lighter ($\dot{M} \sim 10^{-4}\,M_\odot\,\mathrm{yr}^{-1}$) early wind, the cooling frequency reaches IR at times $t_d \sim 30$ d. As a result, injected particles will pile up at the cooling energy. We suggest this as an origin of the late IR bump.[2]

The early X-ray bump should have a separate origin: it cannot be produced by a constant injection source because, in that case, the spectrum will be of the broken power-law type ($\alpha = 0.5$ below the break and $\alpha = p/2$ above the break), not a spectral bump. We suggest that it is produced by an episode of injection; that is, the estimate (28) for the injection energy early on matches the observed spectral peak.

6 LOW-FREQUENCY EMISSION: FREE–FREE ABSORPTION IN THE EJECTA AND THE WIND

At lower frequencies, radio and IR waves can experience free–free absorption (Lang 1999, equation 1.223) both within the ejecta and in the pre-explosion wind.

Ejecta contributes to free–free absorption a lot:

$$\tau_{ff,ej} = 2 \times 10^{20} m_{ej,-2}^4 \nu_{GHz}^{-4.2} T_4^{-2.7} t_d^{-10}. \quad (31)$$

It is optically thin for very high frequencies for a long time:

$$\nu_{GHz} > 7 \times 10^4 m_{ej,0.95} T_4^{-0.64} t_d^{-2.4}. \quad (32)$$

Thus, in the radio and far-IR, the ejecta remains mostly opaque until the shock breakout from the ejecta, after approximately a month (see equation 7).

The free–free optical depth through the wind, with density given by equation (1), becomes unity at

$$r_{ff,wind} = 1.5 \times 10^{16} \dot{m}_{-5}^{2/3} \nu_{GHz}^{-7/10} T_4^{-9/20} v_{w,8}^{-2/3}. \quad (33)$$

The shock (21) reaches the optical depth of the order of unity through the pre-explosion wind (equation 33), for

$$t = 8\,\dot{m}_{-5}^{8/15} \nu_{GHz}^{-14/25} T_4^{-9/25} v_{w,8}^{-8/15} m_{ej,-2}^{1/5}\,\mathrm{d}. \quad (34)$$

The effects of free–free absorption explain the evolution of the radio and IR luminosities (Ho et al. 2019; see their fig. 1). High frequencies (i.e. 341 and 230 GHz) are transparent all along, while the lower frequency (i.e. 34 GHz) traces the expanding radius of the corresponding $\tau = 1$ surface.

7 POPULATION SYNTHESIS

7.1 Pre-merger evolutionary channels

Most calculations of WD–WD mergers are aimed at explaining the Type Ia SNe, thus looking for detonation (for a recent review, see Maoz, Mannucci & Nelemans 2014). Less attention has been given to models that fail to detonate. As we argue, failed SN Ia, which collapse via electron capture, might be related to the FBOTs.

[2]SNe Ia also show IR excess around ∼30 d (e.g. Scalzo et al. 2019, fig. 3). Given quite different environments, we assume that this similarity is superficial.

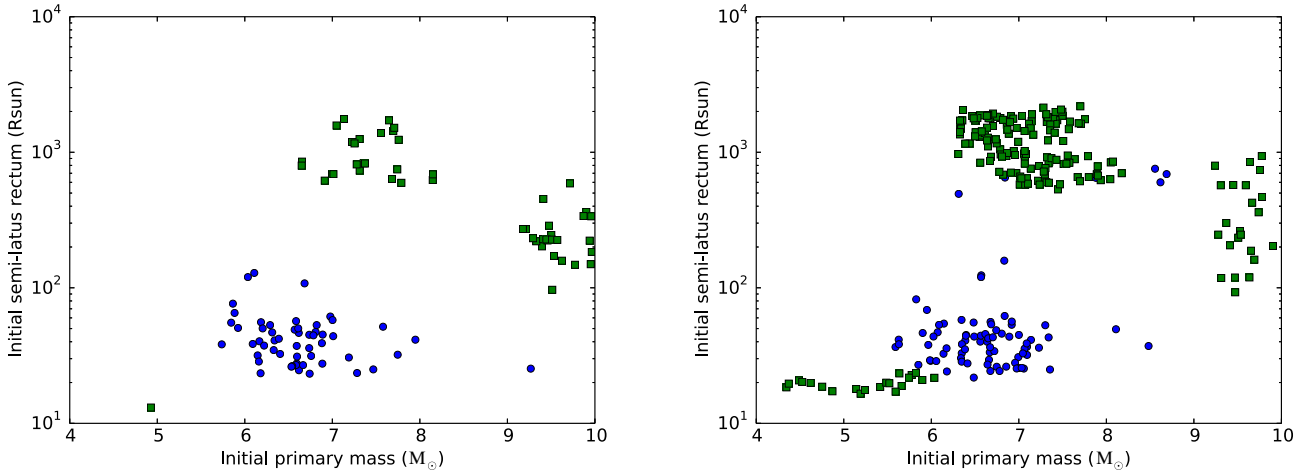

Figure 2. Distribution of initial semi-latus rectum for model $\gamma\alpha$ (left panel) and model $\alpha\alpha$ (right panel). Green squares denote the systems where the ONeMg WD is formed first, and blue circles denote the systems where this is the last formed WD. In all models, the systems marked in blue come from tight orbits where the first phase of mass transfer typically proceeds in a stable manner. The systems marked in green mostly originate from wider orbits, such that that first phase of mass transfer is likely a CE phase. In the case of $\alpha\alpha$, green squares at low orbital separations correspond to the systems in which the primary starts with $\sim$6 $M_\odot$ and relatively small separation, so that the first phase of mass transfer is stable. As the secondary accretes, it becomes more massive, its evolution speeds up, and it becomes a ONeMg WD while the primary is still a stripped (hydrogen-poor helium-rich) nuclear burning star, which eventually becomes a WD. This is similar to the third evolution channel in Toonen et al. (2012).

Dan et al. (2014) discussed the results of the WD–WD mergers and argued that there is large phase space available for WD–WD mergers to produce an AIC. Nomoto & Iben (1985) stressed the role of carbon ignition during WD mergers in order to produce a SN Ia. Thus, in order to avoid an explosion, there should be little carbon in the system. We suggest that the primary is a heavy ONeMg WD. In this section, we calculate possible evolutionary scenarios and rates for the corresponding mergers.

We use the binary population synthesis (BPS) method to predict the properties of the binary mergers (i.e. the merger rates, host galaxies and formation channels). Using the BPS code `SeBa` (Portegies Zwart & Verbunt 1996; Toonen, Nelemans & Portegies Zwart 2012; Toonen & Nelemans 2013), we simulate the evolution of a large number of binaries, following in detail those that lead to the merger of an ONeMg and CO WD. Processes such as wind mass loss, stable and unstable mass transfer, accretion, angular momentum loss and gravitational wave emission are taken into account. It was shown by Toonen et al. (2014) that the main source of uncertainty in the BPS outcomes come from the uncertainty in the input assumptions, in particular the CE phase (CE stands for common envelope). For this reason, we follow Toonen et al. (2012), in performing two sets of population synthesis calculations using their model $\alpha\alpha$ and $\gamma\alpha$. For full details on the models, see Toonen et al. (2012). In short, these models differ from one another with respect to the modelling of the CE phase. Despite the importance of this phase for the formation of compact binaries and the enormous effort of the community, the CE phase is still poorly constrained (for a review, see Ivanova et al. 2013).

Commonly, the CE phase is modelled in BPS codes by energy conservation (Webbink 1984), with a parameter α that describes the efficiency with which orbital energy $E_{\rm orb}$ is consumed to unbind the CE, that is,

$$\frac{GM_{\rm d}M_{\rm d,\,env}}{\lambda R} = \alpha_{\rm CE}(E_{\rm orb,\,init} - E_{\rm orb,\,final}),$$

where $M_{\rm d}$ is the mass of the donor star, $M_{\rm d,env}$ is the mass of its envelope and R is its radius, and λ is the structure parameter of its envelope (Paczynski 1976; Webbink 1984; de Kool, van den Heuvel & Pylyser 1987; Livio & Soker 1988; de Kool 1990). This recipe is used in model $\alpha\alpha$ for every CE phase with $alpha * lambda = 2$ (Nelemans et al. 2000).

This model is based on a balance of angular momentum with an efficiency parameter γ defined as

$$\frac{J_{\rm init} - J_{\rm final}}{J_{\rm init}} = \frac{\gamma M_{\rm d,\,env}}{M_{\rm d} + M_{\rm a}},$$

where $J_{\rm init}$ and $J_{\rm final}$ denote the angular momentum of the pre- and post-mass transfer binary, respectively, and $M_{\rm a}$ is the mass of the companion. This model is based on a balance of angular momentum with an efficiency parameter $\gamma = 1.5$ (Nelemans et al. 2000).

Figs 2 and 3 show the initial parameters of binaries leading to mergers between ONeMg and CO WDs in our simulations. Every point represents a single system in the BPS simulations. There are different evolutionary paths that can lead to an ONe–CO WD merger, but the two dominant channels of systems are: (i) the inverted channel (blue circles) consisting of systems with small initial semi-latus rectum $p \equiv a(1 - e^2) < 200R_\odot$ for which the first phase of mass transfer is stable; (ii) systems in the direct channel (green squares) are initially wider and evolve through a CE phase. Typically, the ONeMg–WD forms before the companion WD, whereas in the inverted channel the ONeMg WD is formed last (hence the name). For single stars, the initial mass of the progenitor of an ONeMg WD ranges between approximately 6.5 and 8 $M_\odot$ according to `SeBa`.This is similar to the range of initial masses in the direct channel where the initially most massive star (i.e. primary) forms the ONeMg WD (majority of green points in Fig. 3). The progenitors of ONeMg WDs in the inverted channel (i.e. the initially less massive star or secondary, denoted in blue) have lower masses initially, as these stars accrete a significant amount of mass from their companion stars.

Fig. 4 shows the final masses of the ONeMg and CO WD that merge according to model $\alpha\alpha$ and $\gamma\alpha$, respectively. The masses of

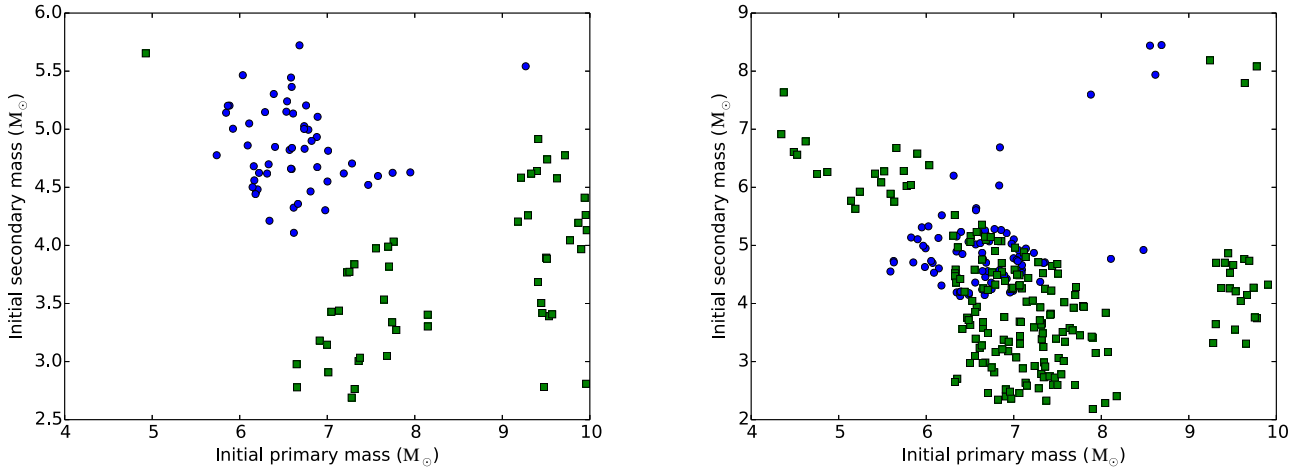

Figure 3. Distribution of initial masses for model $\gamma\alpha$ (left panel) and model $\alpha\alpha$ (right panel). The primary represents the first formed WD, and the secondary the last formed WD. The colour coding is the same as in Fig. 2.

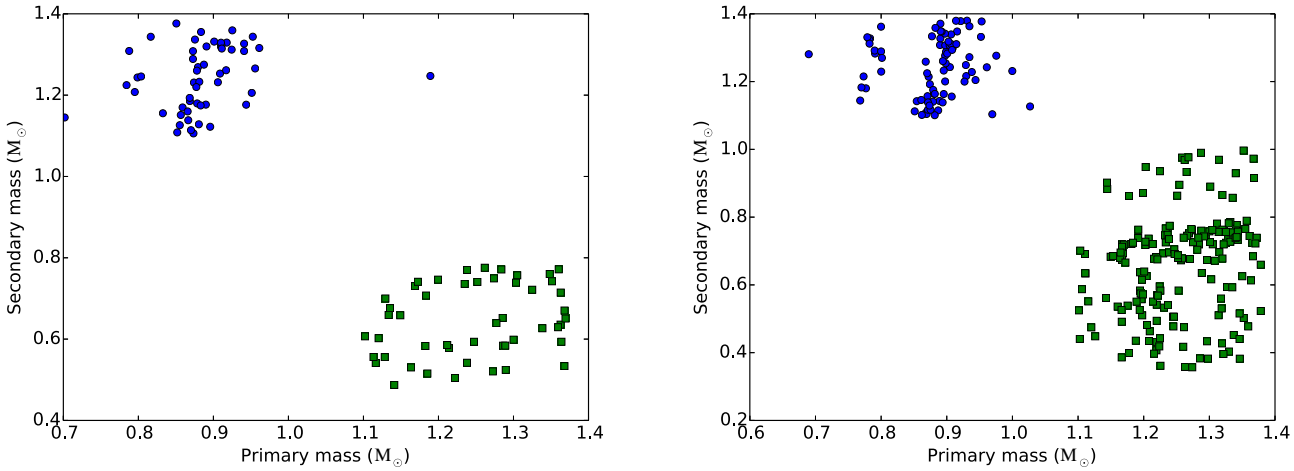

Figure 4. Distribution of WD masses for model $\gamma\alpha$ (left panel) and model $\alpha\alpha$ (right panel). The colour coding is the same as in Fig. 2.

the ONeMg WDs are in the range 1.1–1.4 $M_\odot$, while the majority of CO WDs have masses in the range 0.5–0.8 $M_\odot$. As described above, it is possible that the ONeMg WD forms before the other WD in the system (the direct channel), or it forms afterwards (the inverted channel). In model $\gamma\alpha$, 48 per cent of merging ONe–CO WDs go through the direct channel, whereas for model $\alpha\alpha$ the fraction goes up to 69 per cent. The masses of the CO WDs in the inverted channel are systematically higher than those of the direct channel.

Fig. 5 shows the distribution of the mass ratio as a function of the primary mass at time of merger. For donor masses in the range 1.1–1.3 $M_\odot$, Marsh et al. (2004) (see their fig. 1) find that mass transfer is always unstable if the companion mass is above ∼0.6. It is always stable for ≤0.2–0.4. The blue systems are well above the limit for unstable mass transfer. The green systems occupy a larger part of parameter space. The large majority of the systems have a mass ratio that make stable mass transfer unlikely. Also note that given the optimistic stability limits of Marsh et al. (2004) the AM CVn rate is overestimated by orders of magnitude, indicating that mass transfer is likely less stable than the optimistic scenario. In addition, the results from Marsh et al. (2004) do not take into account the effect of novae outbursts on the evolution of the systems. As shown by Shen et al. (2012), these outbursts have a destabilizing effect on the mass transfer.

7.2 Rates

Using the BPS simulations, we also estimate the rate of CO–ONeMg WD mergers. Assuming a constant star formation history of 4 $M_\odot$ yr^{-1} for a Hubble time (roughly like the Milky Way), the current merger rate ranges from 1.4×10^{-4} yr^{-1} for model $\alpha\gamma$ to 3.4×10^{-4} yr^{-1} for model $\alpha\alpha$. This is in agreement with the BPS calculations of Yungelson & Kuranov (2017) and Ruiter et al. (2019). The CO–ONeMg mergers are less common than mergers between CO–CO WDs for which we find a merger rate of 4.5×10^{-3} yr^{-1}. Mergers of CO–CO WDs with a combined mass above the Chandrasekhar limit, the double-degenerate progenitors model for SN Ia (Iben & Tutukov 1984; Webbink 1984), have a merger rate of 1.7–2.2 $\times$ 10^{-3} yr^{-1} in our simulations, about an order of magnitude above that of CO–ONeMg WDs.

Integrated over time, the total number of CO–ONeMg WD mergers ranges between 3.5 and 8.6 $\times$ 10^{-5} per solar mass of

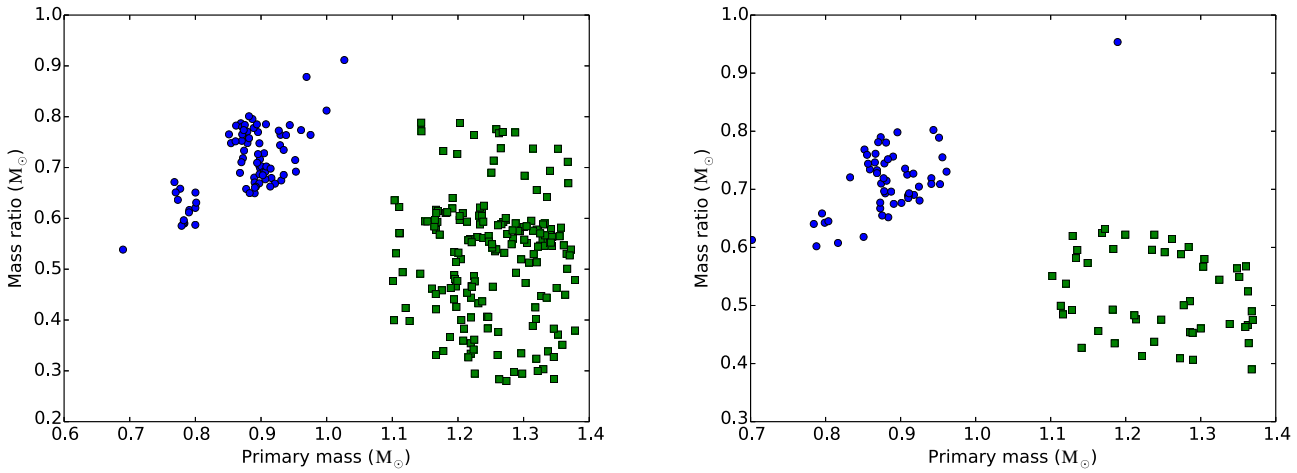

Figure 5. Distribution of the mass ratio as a function of the primary mass for model $\gamma\alpha$ (left panel) and model $\alpha\alpha$ (right panel). The colour coding is the same as in Fig. 2.

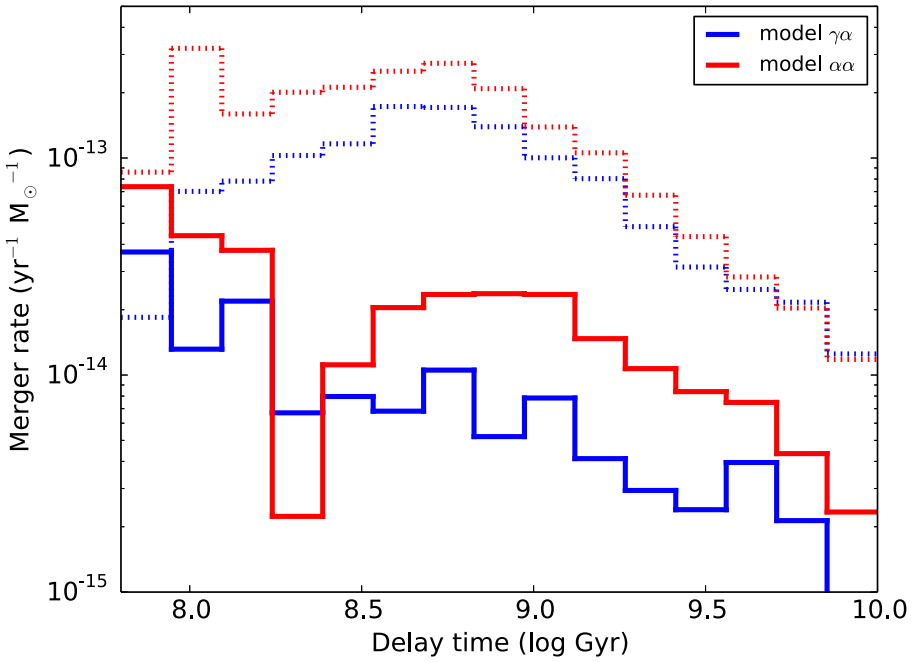

Figure 6. Delay time distribution of the CO–ONeMg WD mergers (solid lines) for two models of CE evolution. Model $\gamma\alpha$ is shown is blue, and model $\alpha\alpha$ in red. For comparison, the super-Chandrasekhar mergers of CO–CO WDs are shown with dotted lines. These typically occur at later delay times than the CO–ONeMg WD mergers.

created stars.[3] The rate of FBOTs has been estimated by Drout et al. (2014) to be 4–7 per cent of core-collapse SNe. Assuming the core-collapse rate is about 0.0025–0.010 $M_\odot^{-1}$ (Horiuchi et al. 2011; Graur et al. 2017; Maoz & Graur 2017),[4] the estimated CO–ONeMg WD merger rate is consistent with the lower limit of the FBOT rate.

[3]This is independent of the assumed star formation history.
[4]The upper limit is calculated by Maoz & Graur (2017). The lower limit is based on the observed SN Ia rate, $(1.3 \pm 0.1) \times 10^{-3}$ $M_\odot^{-1}$ (Maoz & Graur 2017) and the ratio of core-collapse to SNe Ia, 0.25–4 (Graur et al. 2017).

7.3 Host galaxies

Fig. 6 shows the distributions of delay times of the CO–ONeMg mergers after a single burst of star formation. Their merger rates peak at short delay times of about ∼50–100 Myr, with a long tail to long delay times. The peak occurs significantly earlier than expected from the classical SN Ia progenitors consisting of super-Chandrasekhar mergers of CO–CO WDs (consistent with Yungelson & Kuranov 2017; Ruiter et al. 2019). The typical delay time of the CO–ONeMg mergers is closer to that of core-collapse SNe, which peaks sharply at ∼50 Myr (see, e.g., fig. 3 of Zapartas et al. 2017). As a result, we expect the host galaxies of CO–ONeMg mergers to be more similar to those of core-collapse SNe instead of

SNe Ia. This is consistent with the observed host galaxies of FBOTs (Drout et al. 2014).

8 ALTERNATIVES

An alternative to the WD merger scenario is the possibility of ultra-stripped envelopes in close binaries (Tauris et al. 2013; Tauris, Langer & Podsiadlowski 2015). Binary interactions can strip the primary star of the envelope and also affect the mass of the collapsing core (Podsiadlowski et al. 2004; Langer 2012). Müller et al. (2018, 2019) estimate that ultra-stripped SNe produce normal slowly rotating pulsars, which are unlikely to produce a fast spinning central NS. Müller et al. (2018) studied the case when the angular momentum is implanted on to the NS only due to accretion of a tenuous envelope, without accounting for the progenitor's initial spins. In contrast, in the case of double WD merger, the envelope has a lot of angular momentum and has time to implant it to the core during the shell-burning stage.

In a possibly related line of research, Piran & Shaviv (2005) – see also Dall'Osso, Piran & Shaviv (2014) – argued that the pulsar J0737–3039B was born through a non-standard SN mechanism (presumably via AIC), similar to the ultra-stripped case considered by Tauris et al. (2015). Piran & Shaviv (2005) also argued for slow initial spin (and slow kick velocity). Thus, ultra-stripped binary cores produce slowly rotating remnants, while AT2018cow needs a powerful central source.

9 DISCUSSION

In this paper, we discuss a channel for transient emission after electron-capture collapse to a NS following a merger of two WDs. Qualitatively, this channels allows a collapse into a NS to occur with a small envelope mass. As a result, the ejecta is light, has high velocity and becomes optically transparent much earlier. This early transparency allows higher radiation efficiency, as energy is not spent on adiabatic expansion of the envelope. In AT2018cow, the ejecta was the lightest, with only $\sim 10^{-2}\,\mathrm{M}_\odot$ ejected. In this case, the AIC occurred at the time when most of the envelope was already lost to the wind. Other FBOTs can have larger remaining envelopes at the moment of AIC and larger ejected masses, but all smaller than $\sim 0.5\,\mathrm{M}_\odot$. In our model, the envelope mass depends on the mass of the primary ONeMg WD (how close it is to the Chandrasekhar limit), and the mass of the companion (how quickly mass is added to the core, mass loss rate, i.e. how long the shell burning continues).

Let us highlight how the key observational results discussed by Margutti et al. (2019) are explained in our model.

(i) A very short rise time to peak, $t_{\rm rise} \sim$ few days: the optical transient is generated by an envelope ejected during the bounce from the proto-NS. Ejected mass is small, while velocity is nearly relativistic (of the order of the escape velocity from the surface of a proto-NS).

(ii) Large bolometric peak luminosity: as the ejecta becomes optically thin early on, a large fraction of the internal energy is emitted (as opposed to being spent on adiabatic expansion in a conventional SN explosion).

(iii) Persistent blue colours, with lack of evidence for cooling at $\delta t \gtrsim 30$ d: later, the emission starts to become dominated by the non-thermal particle accelerators at the termination shock.

(iv) Large blackbody radius $R_{\rm bb} \sim 8 \times 10^{14}$ cm: wind-driven cavity expands to these scales on time-scales of a few days (equation 21).

(v) Persistent optically thick UV/optical emission with no evidence for transition into a nebular phase: emission is dominated by the radiation-modified forward shock.

(vi) Abrupt change of the velocity of the material, which dominates the emission at times $\geq$20 d: the jet breaks through the ejecta and enters the pre-explosion wind, after time given by equation (7).

(vii) NIR excess of emission: the cooling energy at the termination shock moved to IR both due to the decreasing magnetic field in the post-shock flow (equation 28) and discussion afterwards.

(viii) The spectra evolve from a hot, blue and featureless continuum around the optical peak, to very broad features: this is a transition from radiation-modified forward shock at early time to regular matter-dominated forward shock, combined with emission from the termination shock.

In addition, we note the following.

(i) 'Late-time optical spectra at $t > 20$ d show linewidths of 4000 km s^{-1} (0.01c, indicating substantially lower outflow velocities than at earlier times (when $v = 0.1$c), and an abrupt transition from very high velocity to lower velocity emitting material' (Margutti et al. 2019). We associate this transition with the moment when the NS-driven shock ploughs through the ejecta and enters the pre-collapse wind (equation 7). This is due to slowing down of the ejecta.

(ii) There are indications of hydrogen in the spectrum after a few weeks (Margutti et al. 2019): if the disrupted WD was of the DA type, one does expect of the order of $10^{-4}\,\mathrm{M}_\odot$ of hydrogen in the pre-collapse wind. This explains the late appearance of hydrogen lines, presumably when the NS-driven forward shock exits the ejecta and enters the pre-existing wind. We have no way of telling what the atmosphere of a post-interaction WD will be. However, it is probable that the majority will be a DA, and therefore the rates would not be wildly different from the ones presented here. Also, in a DA WD hydrogen is limited to a narrow outer layer that will be stripped first during the merger and then mixed up in the envelope.

(iii) Similar X-ray and optical luminosities are naturally explained as emission from forward and NS wind termination shocks (the latter in the fast cooling regime).

(iv) The early X-ray spectral bump is also due to the passage of the peak frequency (a late similar effect will produce an IR increase)

(v) Erratic inter-day variability of the X-ray emission (Ho et al. 2019) is hard to reproduce within the forward shock scenario (Lyutikov 2006b), since the forward shock emission properties depend on the *integrated* quantities (central engine total energy and total matter swept). But this variability can be reproduced within the internal shock paradigm: in the fast cooling regime, either by the changes of the wind properties of the central source (Lyutikov & Camilo Jaramillo 2017), minijets in the outflow (Lyutikov 2006a), or by Crab flare-like reconnection processes in the shocked pulsar wind (Clausen-Brown & Lyutikov 2012; Lyutikov et al. 2018).

(vi) We associate both the high energy as well as radio emission not with the forward shock, as is the case in regular SNe (Weiler et al. 1986; Chevalier 1998), but with the reverse shock in the newly formed PWN. As a result, temporal evolution will be different.

Also note that AIC with a formation of a NS is probably responsible for the formation of young pulsars in globular clusters (Lyne, Manchester & D'Amico 1996). This is consistent with the present model.

The present model, connecting FBOTs to the merger of WDs, is related to the possibility that *some* short GRBs come from a similar channel of WD mergers (Lyutikov & Toonen 2017). The detection of gravitational waves associated with a GRB (Abbott et al. 2017) identifies NS mergers as the central engine. It is not clear at the moment whether this identification is generic to the whole class of short GRBs. As discussed by Lyutikov (2009) and Lyutikov & Toonen (2017), there are a number of observational contradictions to the binary NS merger paradigm (e.g. extended emission and late flares, neither seen in GW/GRB170817). One possibility that is still viable is that some short GRBs originate from WD mergers. Several parameters might be separate outcomes of WD mergers (e.g. FBOTs and short GRBs): masses of the merging WDs, the amount of the material lost to the wind, and the spin right before the AIC (so that AIC can either occur directly to a NS or with the formation of an accretion disc). For preferential intrinsic parameters and viewing angles (e.g. an observer along the spin axis of the collapsing WD), we can see a short GRB and, later, an FBOT.

ACKNOWLEDGEMENTS

This work had been supported by DoE grant DE-SC0016369 and NASA grant 80NSSC17K0757. We would like to thank Maxim Barkov, Deanne Coppejans, Robert Fisher, Ori Fox, Raffaella Margutti, Danny Milisavljevic, Amir Levinson, Eran Ofek, Amir Sharon, Liliana Rivera, Nir Shaviv and Thomas Tauris for discussions. We also thank Yegor Lyutikov for comments.

REFERENCES

Abbott B. P. et al., 2017, Phys. Rev. Lett., 119, 161101
Abdikamalov E. B., Ott C. D., Rezzolla L., Dessart L., Dimmelmeier H., Marek A., Janka H.-T., 2010, Phys. Rev. D, 81, 044012
Arnett W. D., 1982, ApJ, 253, 785
Balsara D. S., Fisker J. L., Godon P., Sion E. M., 2009, ApJ, 702, 1536
Belyaev M. A., Rafikov R. R., Stone J. M., 2013, ApJ, 770, 67
Bisnovatyi-Kogan G. S., Silich S. A., 1995, Rev. Mod. Phys., 67, 661
Brooks J., Schwab J., Bildsten L., Quataert E., Paxton B., Blinnikov S., Sorokina E., 2017, ApJ, 850, 127
Budnik R., Katz B., Sagiv A., Waxman E., 2010, ApJ, 725, 63
Canal R., Schatzman E., 1976, A&A, 46, 229
Chevalier R. A., 1998, ApJ, 499, 810
Clausen-Brown E., Lyutikov M., 2012, MNRAS, 426, 1374
Dall'Osso S., Piran T., Shaviv N., 2014, MNRAS, 438, 1005
Dan M., Rosswog S., Brüggen M., Podsiadlowski P., 2014, MNRAS, 438, 14
de Kool M., 1990, ApJ, 358, 189
de Kool M., van den Heuvel E. P. J., Pylyser E., 1987, A&A, 183, 47
Drout M. R. et al., 2014, ApJ, 794, 23
Fryer C., Benz W., Herant M., Colgate S. A., 1999, ApJ, 516, 892
Graur O. et al., 2017, ApJ, 837, 120
Höflich P., Wheeler J. C., Thielemann F. K., 1998, ApJ, 495, 617
Horiuchi S., Beacom J. F., Kochanek C. S., Prieto J. L., Stanek K. Z., Thompson T. A., 2011, ApJ, 738, 154
Ho A. Y. Q. et al., 2019, ApJ, 871, 73
Iben, Jr. I., Tutukov A. V., 1984, ApJS, 54, 335
Inogamov N. A., Sunyaev R. A., 1999, Astron. Lett., 25, 269
Inogamov N. A., Sunyaev R. A., 2010, Astron. Lett., 36, 848
Ioka K., Levinson A., Nakar E., 2019, MNRAS, 484, 3502
Ito H., Levinson A., Stern B. E., Nagataki S., 2018, MNRAS, 474, 2828
Ivanova N. et al., 2013, A&AR, 21, 59
Jones S., Röpke F. K., Pakmor R., Seitenzahl I. R., Ohlmann S. T., Edelmann P. V. F., 2016, A&A, 593, A72
Karp A. H., Lasher G., Chan K. L., Salpeter E. E., 1977, ApJ, 214, 161
Kashyap R., Haque T., Lorén-Aguilar P., García-Berro E., Fisher R. T., 2018, ApJ, 869, 140
Kitaura F. S., Janka H.-T., Hillebrandt W., 2006, A&A, 450, 345
Kompaneets A. S., 1960, Sov. Phys. Dokl., 5, 46
Landau L. D., Lifshitz E. M., 1959, Fluid Mechanics. Pergamon Press, Oxford
Langer N., 2012, ARA&A, 50, 107
Lang K. R., 1999, Astrophysical Formulae. Springer, Berlin
Livio M., Soker N., 1988, ApJ, 329, 764
Lyne A. G., Manchester R. N., D'Amico N., 1996, ApJ, 460, L41
Lyutikov M., 2006a, MNRAS, 369, L5
Lyutikov M., 2006b, New J. Phys., 8, 119
Lyutikov M., 2009, preprint (arXiv:0911.0349)
Lyutikov M., 2018, MNRAS, 477, 816
Lyutikov M., Camilo Jaramillo J., 2017, ApJ, 835, 206
Lyutikov M., Toonen S., 2017, preprint (arXiv:1709.02221)
Lyutikov M., Komissarov S., Sironi L., 2018, J. Plasma Phys., 84, 635840201
Maoz D., Graur O., 2017, ApJ, 848, 25
Maoz D., Mannucci F., Nelemans G., 2014, ARA&A, 52, 107
Margutti R. et al., 2019, ApJ, 872, 18
Marsh T. R., Nelemans G., Steeghs D., 2004, MNRAS, 350, 113
Michel F. C., 1973, ApJ, 180, L133
Miyaji S., Nomoto K., Yokoi K., Sugimoto D., 1980, PASJ, 32, 303
Mösta P., Ott C. D., Radice D., Roberts L. F., Schnetter E., Haas R., 2015, Nature, 528, 376
Müller B., Gay D. W., Heger A., Tauris T. M., Sim S. A., 2018, MNRAS, 479, 3675
Müller B. et al., 2019, MNRAS, 484, 3307
Nelemans G., Verbunt F., Yungelson L. R., Portegies Zwart S. F., 2000, A&A, 360, 1011
Nomoto K., Kondo Y., 1991, ApJ, 367, L19
Nomoto K., Iben I. Jr., 1985, ApJ, 297, 531
Ofek E. O. et al., 2010, ApJ, 724, 1396
Paczynski B., 1976, in Eggleton P., Mitton S., Whelan J., eds, Proc. IAU Symp. Vol. 73, Structure and Evolution of Close Binary Systems. Kluwer, Dordrecht, p. 75
Perley D. A. et al., 2019, MNRAS, 484, 1031
Philippov A. A., Rafikov R. R., Stone J. M., 2016, ApJ, 817, 62
Pinto P. A., Eastman R. G., 2000, ApJ, 530, 757
Piran T., 2004, Rev. Mod. Phys., 76, 1143
Piran T., Shaviv N. J., 2005, Phys. Rev. Lett., 94, 051102
Podsiadlowski P., Langer N., Poelarends A. J. T., Rappaport S., Heger A., Pfahl E., 2004, ApJ, 612, 1044
Portegies Zwart S. F., Verbunt F., 1996, A&A, 309, 179
Prentice S. J. et al., 2018, ApJ, 865, L3
Rivera Sandoval L. E., Maccarone T. J., Corsi A., Brown P. J., Pooley D., Wheeler J. C., 2018, MNRAS, 480, L146
Ruiter A. J., Ferrario L., Belczynski K., Seitenzahl I. R., Crocker R. M., Karakas A. I., 2019, MNRAS, 484, 698
Scalzo R. A. et al., 2019, MNRAS, 483, 628
Schwab J., Quataert E., Bildsten L., 2016, MNRAS, 458, 3613
Sharon A., Kushnir D., 2019, preprint (arXiv:1904.08427)
Shen K. J., Bildsten L., Kasen D., Quataert E., 2012, ApJ, 748, 35
Smartt S. J. et al., 2018, Astron. Telegram, 11727,
Svirski G., Nakar E., 2014, ApJ, 788, 113
Tauris T. M., Langer N., Moriya T. J., Podsiadlowski P., Yoon S-C., Blinnikov S. I., 2013, ApJ, 778, L23
Tauris T. M., Langer N., Podsiadlowski P., 2015, MNRAS, 451, 2123
Timmes F. X., Woosley S. E., 1992, ApJ, 396, 649
Toonen S., Nelemans G., 2013, A&A, 557, A87
Toonen S., Nelemans G., Portegies Zwart S., 2012, A&A, 546, A70
Toonen S., Claeys J. S. W., Mennekens N., Ruiter A. J., 2014, A&A, 562, A14
Toonen S., Perets H. B., Igoshev A. P., Michaely E., Zenati Y., 2018, A&A, 619, A53
Weaver T. A., 1976, ApJS, 32, 233

Webbink R. F., 1984, ApJ, 277, 355
Weiler K. W., Sramek R. A., Panagia N., van der Hulst J. M., Salvati M., 1986, ApJ, 301, 790
Woosley S. E., Baron E., 1992, ApJ, 391, 228
Yungelson L. R., Kuranov A. G., 2017, MNRAS, 464, 1607
Zapartas E. et al., 2017, A&A, 601, A29

APPENDIX A: SEDOV APPROXIMATION FOR DYNAMICS OF PULSAR-DRIVEN WIND PROPAGATING THROUGH PRE-EXPLOSION WIND

Another analytical scaling for the dynamics of the strong shock is the Sedov approximation, which assumes energy conservation (as opposed to momentum flux conservation in the case of the Kompaneets approximation). Consider, first, times shorter than the spin-down time $t \ll t_\Omega$. In the thin shell limit, the energy in the swept-up shell is the energy deposited into the shell by the central source, $L_0 t$, plus the kinetic energy of the swept-up matter $M_{\rm swept} v_{\rm w}^2/2$, where $M_{\rm swept} = 4\pi r r_0^2 \rho_0$ is the swept-up mass (assuming cold wind with constant velocity),

$$L_0 t + 4\pi r r_0^2 v_{\rm w}^2 \rho_0 = 4\pi r r_0^2 \rho_0 v^2/2. \tag{A1}$$

Dimensionalizing

$$\begin{aligned} L_0 &= l_0 2\pi r_0^3 v_{\rm w}^2/2 \\ t &= \tilde{t}(r_0/v_{\rm w}) \\ r &= \tilde{r} r_0, \end{aligned} \tag{A2}$$

we find

$$l_0 \tilde{t} + \tilde{r} = \tilde{r}\dot{\tilde{r}}^2. \tag{A3}$$

At the early time, neglecting the accumulated energy of the wind, $l_0 \tilde{t} \gg \tilde{r}$

$$\begin{aligned} \tilde{r} &= l_0^{1/3} \tilde{t} \\ r &= \frac{{L_0}^{1/3} t}{2\pi^{1/3} {\rho_0}^{1/3} r_0^{2/3}} = \frac{2^{1/3} L_0^{1/3} v_{\rm w}^{1/3}}{\dot{M}^{1/3}} t \end{aligned} \tag{A4}$$

$$V_{\rm s,S} \approx \frac{L_0^{1/3} v_{\rm w}^{1/3}}{\dot{M}^{1/3}}.$$

Comparing with the Kompaneets approximation, we have

$$\frac{V_{\rm s}}{V_{\rm s,S}} \approx c^{1/2} \left(\frac{\dot{M}}{L_0 v_{\rm w}}\right)^{1/6} = 3.6 \dot{M}_{-3}^{1/6} v_{\rm w,8}^{-1/6}. \tag{A5}$$

Thus, both the Sedov and Kompaneets approximations give similar estimates for the shock dynamics at this time.

At times much longer than the spin-down time, $t \gg t_\Omega$, the central engine has deposited most of its energy in the shock, so that energy conservation gives

$$E_0 + 4\pi r r_0^2 v_{\rm w}^2 \rho_0 = 4\pi r r_0^2 \rho_0 v^2/2, \tag{A6}$$

with $E_0 = L_0 t_\Omega$. Dimensionalizing

$$\epsilon_0 = \frac{E_0}{4\pi r_0^3 v_{\rm w}^2/2}, \tag{A7}$$

the energy conservation now takes the form

$$\begin{aligned} \epsilon_0 + \tilde{r} &= \tilde{r}\dot{\tilde{r}}^2 \\ \epsilon_0 &= \frac{E_0}{4\pi r_0^3 v_{\rm w}^2/2}, \end{aligned} \tag{A8}$$

with a solution

$$\tilde{t} = \sqrt{\tilde{r}(\epsilon_0 + \tilde{r})} + \epsilon_0 \ln \frac{\sqrt{\epsilon_0}}{\sqrt{\tilde{r}} + \sqrt{\epsilon_0 + \tilde{r}}}. \tag{A9}$$

At times when the swept-up kinetic energy is not significant,

$$\begin{aligned} \tilde{r} &= (3/2)^{2/3} \epsilon_0^{1/3} \tilde{t}^{2/3} \\ r &= \frac{3^{2/3} {E_0}^{1/3} t^{2/3}}{2\pi^{1/3} {\rho_0}^{1/3} r_0^{2/3}} = \frac{3^{2/3}}{2^{1/3}} \frac{E_0^{1/3} v_{\rm w}^{1/3}}{\dot{M}^{1/3}} t^{2/3}, \end{aligned} \tag{A10}$$

where the last two relations assume a limit of $r \to 0$.

This paper has been typeset from a TEX/LATEX file prepared by the author.